

Supporting Information for

Disphenoidal zero-dimensional lead, tin, and germanium halides: highly emissive singlet and triplet self-trapped excitons and X-ray scintillation

Viktoriia Morad,^{†‡} Yevhen Shynkarenko,^{†‡} Sergii Yakunin,^{†‡} Alexandra Brumberg,[#] Richard D. Schaller,^{#,§} and Maksym V. Kovalenko^{†,‡,*}

[†] Laboratory of Inorganic Chemistry, Department of Chemistry and Applied Bioscience, ETH Zürich, Vladimir Prelog Weg 1, CH-8093 Zürich, Switzerland

[‡] Laboratory for Thin Films and Photovoltaics, Empa – Swiss Federal Laboratories for Materials Science and Technology, Überlandstrasse 129, CH-8600 Dübendorf, Switzerland

[#] Department of Chemistry, Northwestern University, 2145 Sheridan Rd, Evanston, IL 60208

[§] Center for Nanoscale Materials, Argonne National Laboratory, 9700 Cass Ave, Lemont, IL 60439

*E-mail: mvkovalenko@ethz.ch

1. Materials and Methods

Chemicals. Lead (II) bromide (98%, Acros Organics, 500 g), tin(II) bromide (99.5%, Alfa Aesar, 25 g), germanium(II) bromide (97%, Aldrich-Fine Chemicals, 5 g), tin(II) iodide (99%, Strem Chemicals, 25 g), 1-butyl-1-methylpiperidinium bromide, BmpipBr (>97%, TCI, 5g; 99%, IOLITEC, 50 g), 1-butyl-1-methylpiperidinium iodide, BmpipI (>98%, IOLITEC, 50 g), ethanol, EtOH (anhydrous, 99.8%, Acros Organics, 1 L), dimethylformamide, DMF (anhydrous, 99.8%, Sigma-Aldrich, 100 ml), diethylether, Et₂O (99.5%, extra dry over molecular sieve, stabilized, AcroSeal, 100 ml) were used as received and γ -butyrolactone, GBL (99+%, Acros Organics, 1 L) was additionally dried under vacuum at 110 °C and stored in a glovebox.

Bmpip₂PbBr₄ was prepared by dissolving PbBr₂ (36.7 mg, 0.1 mmol) and BmpipBr (0.4 mmol, 94.5 mg) in DMF (1 ml). Single crystals suitable for X-ray diffraction were grown by a slow diffusion of Et₂O into DMF solution of precursors at room temperature. Crystals were washed with Et₂O and vacuum-dried.

Bmpip₂SnBr₄ was prepared by mixing hot solutions of SnBr₂ (0.4 mmol) and BmpipBr (0.8 mmol) in EtOH (2 ml). The resulting EtOH solution was cooled from 70 °C to room temperature slowly (~5 °C/hour) to form single crystals. The synthesis was carried out in the N₂-filled glovebox with dry solvents. Single crystals were additionally washed with Et₂O and dried under vacuum.

Bmpip₂GeBr₄ was prepared by dissolving BmpipBr (1 mmol) and GeBr₂ (0.5 mmol) in EtOH (3 ml). Subsequent addition of 2 ml of Et₂O resulted in the formation of the white precipitate. For single crystal growth, Et₂O was carefully layered onto EtOH precursor solution and single crystals formed at the interface were collected and vacuum-dried.

Bmpip₂SnI₄ was prepared by dissolving SnI₂ (1 mmol) and BmpipI (2 mmol) in hot GBL (4 ml). After addition of acetone, beige powder (red-luminescent under UV) was collected and vacuum-dried. If an aliquot of a stock GBL solution was set to slowly cool down to RT from 90 °C (~5 °C/hour), single crystals, suitable for X-ray structure determination, were collected.

It is important to mention that Bmpip₂PbBr₄ is stable in ambient conditions displaying no signs of optical properties deterioration after over a year of storage. Bmpip₂SnBr₄ is stable in ambient conditions for over a year but gradually loses QY due to Sn(II) oxidation. Bmpip₂GeBr₄ can be exposed to ambient atmosphere for not more than a day before it completely loses its optical properties due to Ge(II) oxidation. Bmpip₂SnI₄ is less stable than its Br-counterpart, and changes color to red upon brief exposure to air.

2. Characterization

Melting points of Bmpip₂PbBr₄ and Bmpip₂SnBr₄ were determined with BUCHI M-565 Melting point instrument.

Powder X-ray diffraction (XRD) patterns were collected in transmission (Debye-Scherrer geometry) with STADI P diffractometer (STOE & Cie GmbH), equipped with a silicon strip MYTHEN 1K Detector (Fa. DECTRIS) with a curved Ge (111)-Monochromator (CuK_{α1}=1.54056 Å). For the measurement, a grounded powder was placed between the adhesive tape.

Single-crystal XRD measurements were conducted on Bruker Smart Platform diffractometer equipped with a Apex I CCD detector and molybdenum (MoK_α=0.71073 Å) sealed tube as an X-ray source and Oxford Xcalibur S diffractometer equipped with Sapphire 3 CCD detector and molybdenum (MoK_α=0.71073 Å) sealed tube as an X-ray source. Crystals were tip-mounted on a micromount with paraffin oil. The data were processed with Oxford Diffraction CrysAlis Pro software, structure solution and refinement was performed with SHELXS and SHELXL¹ respectively, imbedded in the Olex2² package.

The crystal structure of the synthesized compound was solved with direct methods, light elements (C, N) were located in the difference Fourier map, most of the positions of the cations were refined as rigid groups, and hydrogen atoms were placed at calculated positions. The crystallographic data for the reported Bmpip₂MBr₄ (M = Ge, Sn, Pb) were deposited at the Cambridge Crystallographic Data Centre (CCDC) under the codes 1897911 (Bmpip₂PbBr₄), 1897912 (Bmpip₂SnBr₄), 1897913 (Bmpip₂GeBr₄).

Photoluminescence emission and excitation steady-state spectra were recorded either with FluoroMax4-Plus-P (Horiba Jobin Yvon) or Fluorolog 3 (Horiba Jobin Yvon), equipped with 150 W and 500 W Xenon lamps, respectively. For the Figures 2a-b and S6-8, steady-state PL spectra were collected from samples photoexcited by a 35 ps, 405 nm pulsed diode laser through a fiber optic to a thermoelectrically-cooled CCD.

Temperature dependences of photoluminescence emission (PL) and excitation (PLE) spectra were acquired with FluoTime 300 spectrometer from PicoQuant GmbH coupled with CS204 closed cycle helium cryostat from Advanced Research Systems. Excitation was provided by a Xe lamp (power of 300W), passed through a monochromator and cut at emission monochromator with a 400-nm longpass filter. The temperature of a sample was ramped with a speed of 2 K min⁻¹. Spectra were corrected for the spectral sensitivity of the detector and spectral power density of the lamp. For Figures S6-S8, **streak-camera** temperature-dependent photoluminescence was obtained by mounting the samples in between two sapphires in a helium cryostat. Samples were excited at 300 nm with a repetition rate of 2 kHz. The pump beam was produced by frequency quadrupling the signal output at 1200 nm of an optical parametric amplifier that was pumped with 800 nm, 35 fs pulses of an amplified Ti:sapphire laser. The pump beam was filtered through a 275-375 nm bandpass filter and its power density was maintained at roughly 130 $\mu\text{J}/\text{cm}^2$. Emission from the sample was filtered using two 320 nm longpass filters and directed into either a 0.3 m spectrograph with a thermoelectrically-cooled CCD (for static measurements) or to a 0.15 m spectrograph and a single photon-sensitive streak camera (for time-resolved measurements).

Absolute quantum yields were measured using a Quantaaurus-QY spectrometer from Hamamatsu in powder mode.

Luminescence spectra under X-ray excitation were measured with FluoTime 300 spectrometer from PicoQuant GmbH fiber coupled to the sample irradiated with Amptek Mini-X X-ray Ag tube (50kV, 79 μA). The obtained spectra were corrected to account for the sensitivity of the spectrometer and detector.

A photograph of the fluorescence under X-rays was obtained with Rayme DG-073B-DC X-ray tube as an excitation source (70kV, 1mA, 1.8s exposure time) synced to the Canon EOS 200D camera with Canon EF-S 60mm f/2.8 Macro lens and Hoya Pro 1 Digital UV 52mm filter (estimated cutoff wavelength of 390 nm). The sample was positioned at a ~ 15 cm distance from the X-ray tube.

3. Computation details

Ground state electronic structures were calculated with DFT using Vienna ab-initio simulation package (VASP) code. The projector augmented wave (PAW)³ potentials for atoms were used. For the generalized gradient approximation (GGA), the Perdew-Burke-Ernzerhof exchange-correlation functional (PBE)⁴ was used. A correction for van der Waals interactions was implemented with DFT-D2 method of Grimme with a cutoff radius of 30 Å and damping parameter $d = 20$. A reduced unit cell (half the crystallographic unit cell) comprising two MX_4 anions and four Bmpip cations was used for band structure and density of states (DOS) calculations. The atomic positions were optimized until the forces on atoms were smaller than 0.01 eV/Å. Band structure calculations were performed along the high-symmetry K-points path generated with the density of 20 points. Excited state geometry was calculated with DFT as implemented in the cp2k code. The kinetic energy cutoff of the plane-wave basis was 400 eV. The PAW method was used to describe the interaction between ions and electrons. To find the energy of the excited state, atomic positions were optimized with spin-unrestricted Kohn-Sham approach, setting the spin multiplicity to triplet.⁵ Lattice parameters were fixed at the experimental values and atomic positions were optimized until the force on the atoms was smaller than 4.5E-04 Hartree/bohr (0.023 eV/Å). High-symmetry K-path search, band-structure and DOS plots were prepared using sumo toolkit.⁶

In addition, we have estimated the influence of spin-orbit coupling (SOC) inclusion and post-DFT Hartree-Fock/DFT hybrid functional + SOC treatment on the electronic structure of Bmpip₂MBr₄. Post-DFT Hartree-Fock/DFT hybrid functionals PBE0 and HSE06 with 25% of the exact exchange were used for this purpose.⁷

Table S1. Experimental melting points of Bmpip₂MBr₄.

Bmpip ₂ PbBr ₄	176.6 °C
Bmpip ₂ SnBr ₄	125.6 °C

Table S2. Crystallographic data for Bmpip₂PbBr₄.

Empirical formula	C ₂₀ H ₄₄ Br ₄ N ₂ Pb
Formula weight	839.40
Temperature/K	100
Crystal system	Monoclinic
Space group	C2/c
a/Å	20.3640(9)
b/Å	8.4235(2)
c/Å	18.8888(9)
α/°	90
β/°	123.796(7)
γ/°	90
Volume/Å ³	2692.6(3)
Z	4
ρ _{calc} /cm ³	2.071
μ/mm ⁻¹	12.211
F(000)	1600.0
Crystal size/mm ³	0.19 × 0.19 × 0.19
Radiation	MoKα (λ = 0.71073)
2θ range for data collection/°	4.724 to 62.948
Index ranges	-29 ≤ h ≤ 28, -11 ≤ k ≤ 12, -26 ≤ l ≤ 26
Reflections collected	14568
Independent reflections	4117 [R _{int} = 0.0161, R _{sigma} = 0.0123]
Data/restraints/parameters	4117/0/125
Goodness-of-fit on F ²	1.079
Final R indexes [I ≥ 2σ (I)]	R ₁ = 0.0213, wR ₂ = 0.0501
Final R indexes [all data]	R ₁ = 0.0229, wR ₂ = 0.0508
Largest diff. peak/hole / e Å ⁻³	0.74/-0.60

Table S3. Crystallographic data for Bmpip₂SnBr₄.

Empirical formula	C ₂₀ H ₄₄ Br ₄ N ₂ Sn
Formula weight	750.90
Temperature/K	100
Crystal system	Monoclinic
Space group	C2/c
a/Å	20.122(3)
b/Å	8.4218(6)
c/Å	18.801(2)
α/°	90
β/°	123.374(17)
γ/°	90
Volume/Å ³	2660.7(7)
Z	4
ρ _{calc} /cm ³	1.875
μ/mm ⁻¹	6.977
F(000)	1472.0
Crystal size/mm ³	0.19 × 0.19 × 0.18
Radiation	MoKα (λ = 0.71073)
2θ range for data collection/°	4.77 to 62.838
Index ranges	-29 ≤ h ≤ 28, -12 ≤ k ≤ 12, -27 ≤ l ≤ 27
Reflections collected	14448
Independent reflections	4061 [R _{int} = 0.0278, R _{sigma} = 0.0217]
Data/restraints/parameters	4061/0/125
Goodness-of-fit on F ²	1.132
Final R indexes [I ≥ 2σ (I)]	R ₁ = 0.0339, wR ₂ = 0.0739
Final R indexes [all data]	R ₁ = 0.0396, wR ₂ = 0.0758
Largest diff. peak/hole / e Å ⁻³	1.12/-0.54

Table S4. Crystallographic data for Bmpip₂GeBr₄.

Empirical formula	C ₂₀ H ₄₄ Br ₄ GeN ₂
Formula weight	704.80
Temperature/K	122(3)
Crystal system	Monoclinic
Space group	C2/c
a/Å	20.0807(7)
b/Å	8.42480(10)
c/Å	18.3778(5)
α/°	90

$\beta/^\circ$	121.862(4)
$\gamma/^\circ$	90
Volume/ \AA^3	2640.61(16)
Z	4
$\rho_{\text{calc}}/\text{cm}^3$	2.216
μ/mm^{-1}	9.028
F(000)	1750.0
Crystal size/ mm^3	$0.19 \times 0.19 \times 0.19$
Radiation	MoK α ($\lambda = 0.71073$)
2 Θ range for data collection/ $^\circ$	4.776 to 61.822
Index ranges	$-27 \leq h \leq 28, -12 \leq k \leq 11, -26 \leq l \leq 25$
Reflections collected	20153
Independent reflections	3856 [$R_{\text{int}} = 0.0455, R_{\text{sigma}} = 0.0387$]
Data/restraints/parameters	3856/0/125
Goodness-of-fit on F^2	1.117
Final R indexes [$I \geq 2\sigma(I)$]	$R_1 = 0.0342, wR_2 = 0.0600$
Final R indexes [all data]	$R_1 = 0.0471, wR_2 = 0.0638$
Largest diff. peak/hole / $e \text{\AA}^{-3}$	0.66/-0.48

Table S5. Crystallographic data for Bmpip₂SnI₄.

Empirical formula	C ₂₀ H ₄₄ I ₄ N ₂ Sn
Formula weight	938.86
Temperature/K	120
Crystal system	monoclinic
Space group	C2/c
a/ \AA	21.201(3)
b/ \AA	8.8184(6)
c/ \AA	19.170(3)
$\alpha/^\circ$	90
$\beta/^\circ$	122.421(18)
$\gamma/^\circ$	90
Volume/ \AA^3	3025.5(8)
Z	4
$\rho_{\text{calc}}/\text{cm}^3$	2.061
μ/mm^{-1}	4.935
F(000)	1760.0
Crystal size/ mm^3	$0.2 \times 0.2 \times 0.2$
Radiation	MoK α ($\lambda = 0.71073$)
2 Θ range for data collection/ $^\circ$	4.552 to 62.574
Index ranges	$-30 \leq h \leq 29, -12 \leq k \leq 12, -26 \leq l \leq 27$

Reflections collected	15354
Independent reflections	4594 [Rint = 0.0525, Rsigma = 0.0314]
Data/restraints/parameters	4594/0/126
Goodness-of-fit on F2	1.125
Final R indexes [$I \geq 2\sigma(I)$]	R1 = 0.0448, wR2 = 0.1076
Final R indexes [all data]	R1 = 0.0504, wR2 = 0.1122
Largest diff. peak/hole / e Å ⁻³	1.51/-1.11

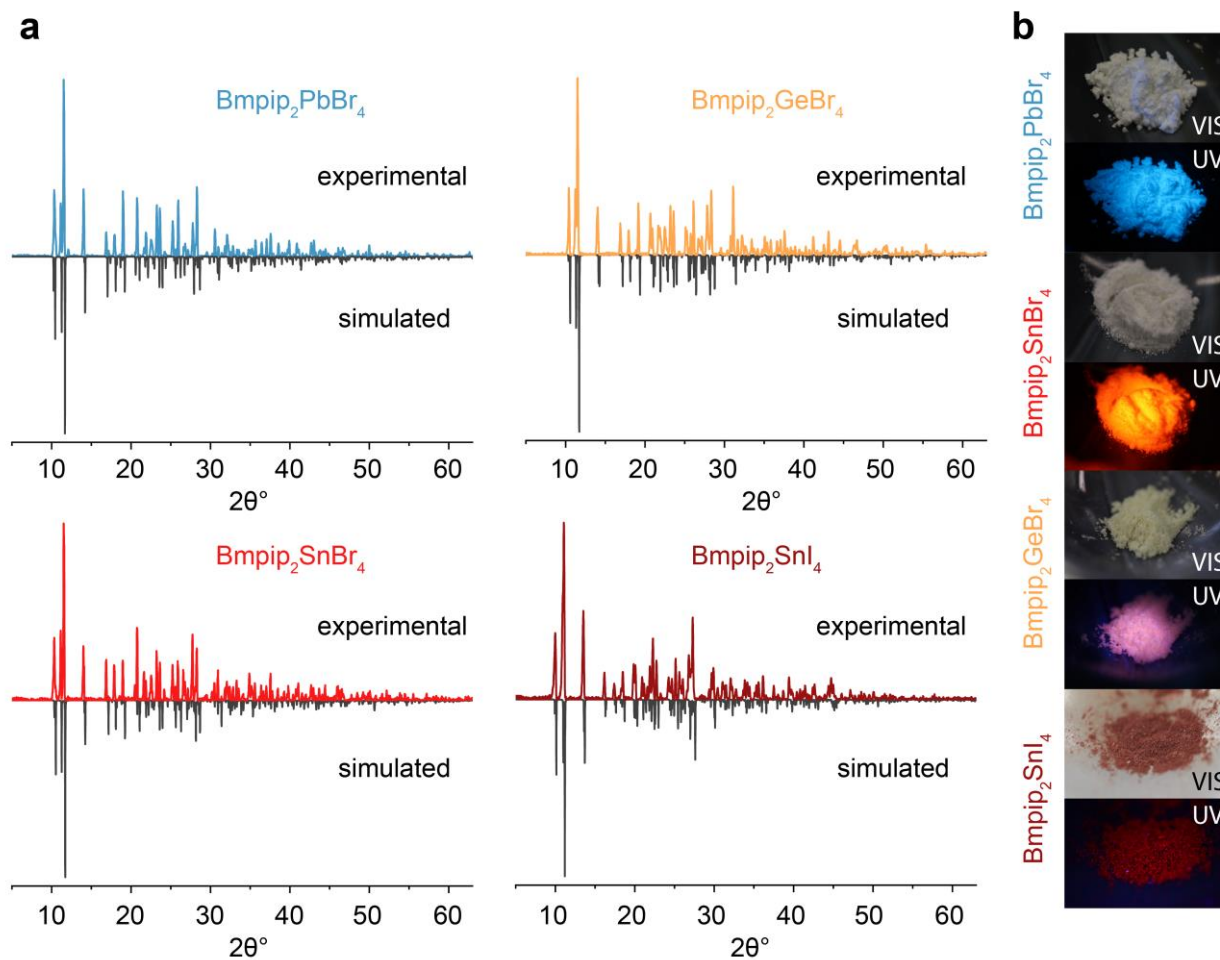


Figure S1. (a) Experimental and simulated powder XRD patterns for $\text{Bmpip}_2\text{SnBr}_4$, $\text{Bmpip}_2\text{PbBr}_4$, $\text{Bmpip}_2\text{SnI}_4$ and $\text{Bmpip}_2\text{GeBr}_4$. (b) Photos of powders under ambient and UV irradiation.

Table S6. Bond lengths for Bmpip₂PbBr₄.

Atom	Atom	Length/Å
Pb(1)	Br(1)	3.0087(3)
Pb(1)	Br(1a)	3.0088(3)
Pb(1)	Br(2)	2.7258(3)
Pb(1)	Br(2a)	2.7258(3)

Table S7. Bond Lengths for Bmpip₂SnBr₄

Atom	Atom	Length/Å
Sn(1)	Br(1)	2.9523(4)
Sn(1)	Br(1a)	2.9523(4)
Sn(1)	Br(2)	2.6430(6)
Sn(1)	Br(2a)	2.6430(6)

Table S8. Bond Lengths for Bmpip₂GeBr₄

Atom	Atom	Length/Å
Ge(1)	Br(2)	2.4716(3)
Ge(1)	Br(2a)	2.4716(3)
Ge(1)	Br(1)	2.8679(4)
Ge(1)	Br(2)	2.8679(4)

Table S9. Bond Lengths for Bmpip₂SnI₄

Atom	Atom	Length/Å
Sn(1)	I(1)	3.1780(7)
Sn(1)	I(1a)	3.1780(7)
Sn(1)	I(2)	2.8610(5)
Sn(1)	I(2a)	2.8611(5)

Table S10. Bond Angles for Bmpip₂PbBr₄

Atom	Atom	Atom	Angle/°
Br(1)	Pb(1)	Br(1a)	179.409(10)
Br(2)	Pb(1)	Br(1)	92.005(8)
Br(2a)	Pb(1)	Br(1)	88.377(8)
Br(2)	Pb(1)	Br(1a)	88.378(8)
Br(2a)	Pb(1)	Br(1a)	92.005(8)
Br(2)	Pb(1)	Br(2a)	99.429(13)

Table S11. Bond Angles for Bmpip₂SnBr₄

Atom	Atom	Atom	Angle/°
Br(1a)	Sn(1)	Br(1)	176.419(15)
Br(2)	Sn(1)	Br(1a)	87.177(12)
Br(2)	Sn(1)	Br(1)	90.479(12)
Br(2a)	Sn(1)	Br(1)	87.177(12)
Br(2a)	Sn(1)	Br(1a)	90.477(13)
Br(2)	Sn(1)	Br(2a)	98.21(2)

Table S12. Bond Angles for Bmpip₂SnI₄

Atom	Atom	Atom	Angle/°
I(1)	Sn(1)	I(1a)	179.245(19)
I(2a)	Sn(1)	I(1)	90.575(18)
I(2a)	Sn(1)	I(1a)	88.930(18)
I(2)	Sn(1)	I(1)	88.930(19)
I(2)	Sn(1)	I(1a)	90.575(19)
I(2)	Sn(1)	I(2a)	98.12(2)

Table S13. Bond Angles for Bmpip₂GeBr₄

Atom	Atom	Atom	Angle/°
Br(1)	Ge(1)	Br(1a)	177.010(17)
Br(2)	Ge(1)	Br(2a)	100.068(17)
Br(2)	Ge(1)	Br(1)	89.418(13)
Br(2a)	Ge(1)	Br(1a)	89.418(13)
Br(2)	Ge(1)	Br(1a)	90.502(13)
Br(2a)	Ge(1)	Br(1)	90.502(13)

Table S14. Summary of the optical properties of Bmpip₂MBr₄

Compound	Emission /nm	Excitation /nm	Stokes shift /nm	τ	ϕ
Bmpip ₂ PbBr ₄	470	347	123	66 ns	24 %
Bmpip ₂ SnBr ₄	666	340	326	4 μ s	75 %
Bmpip ₂ GeBr ₄	670	340	330	1.5 μ s	<1 %
Bmpip ₂ SnI ₄	730	410	360	1.9 μ s	35 %

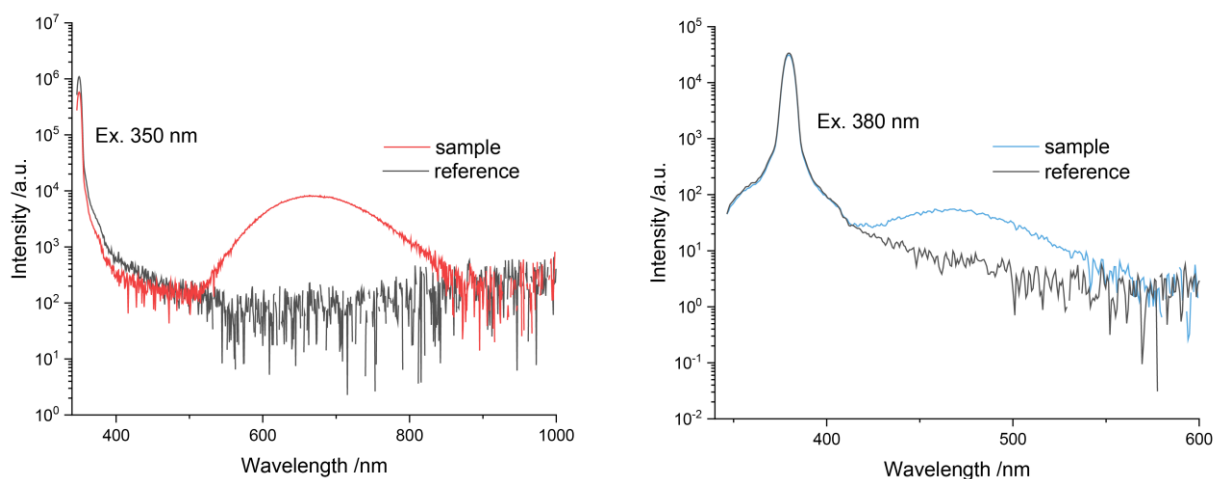


Figure S2. Photoluminescence measurement spectra for Bmpip₂SnBr₄ (red) and Bmpip₂PbBr₄ (blue).

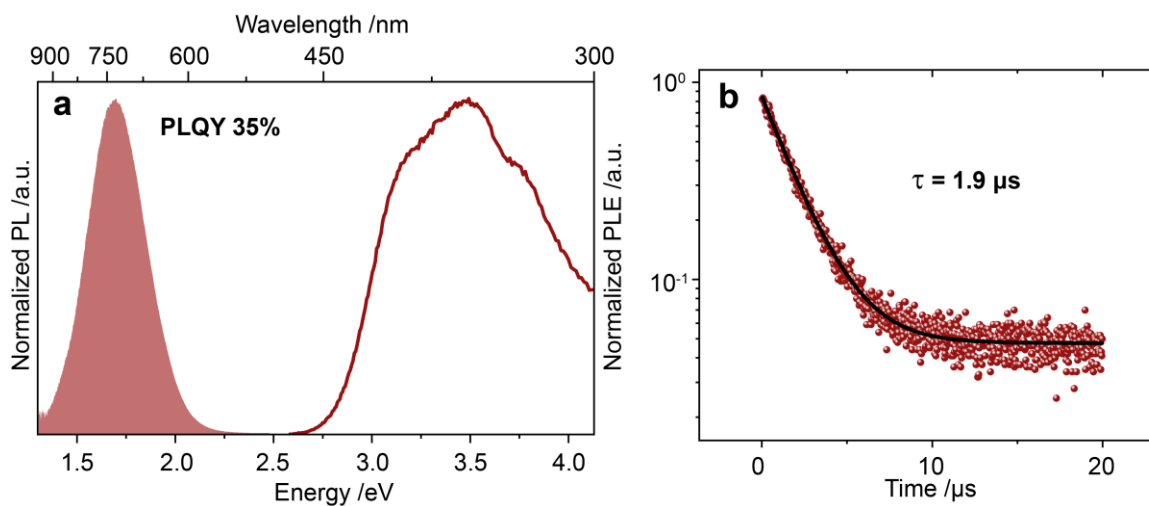


Figure S3. (a) Photoluminescence emission and excitation spectra of Bmpip₂SnI₄. (b) Photoluminescence decay of Bmpip₂SnI₄ and monoexponential fitting.

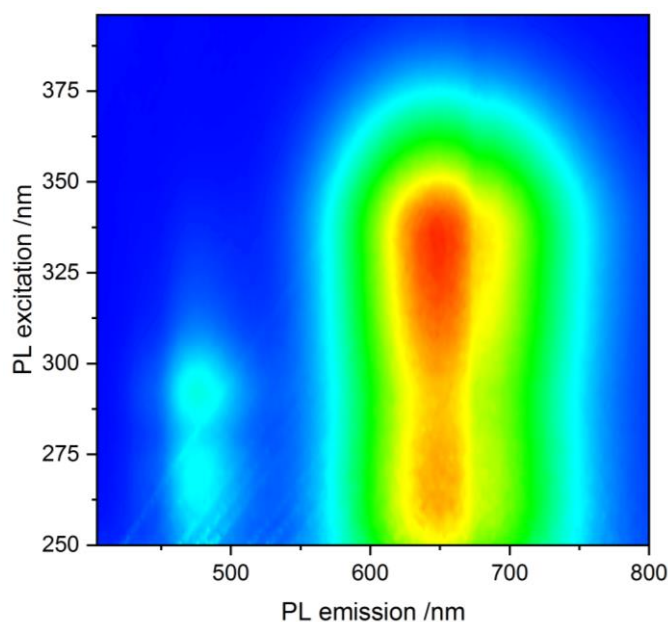


Figure S4. 2D PL vs. PLE map for Bmpip₂SnBr₄ at room temperature. The intensity normalized between 0 and 1. The map shows independent excitation spectra for singlet and triplet emission: triplet emission can be accessed without exciting the singlet band.

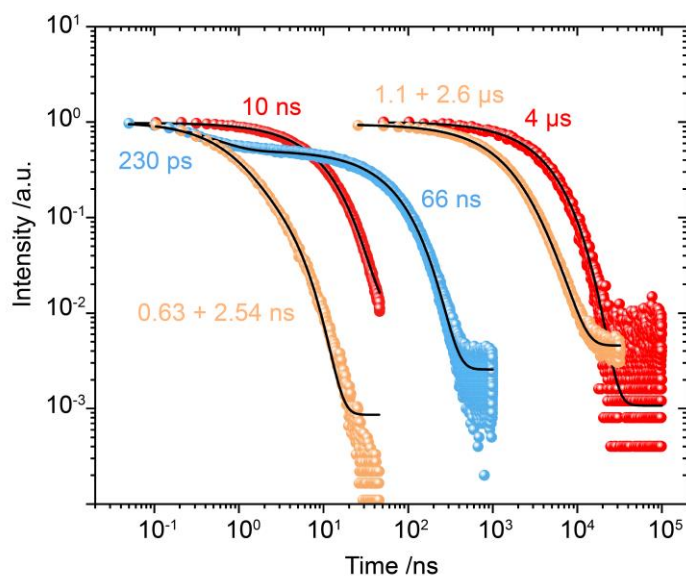


Figure S5. Room-temperature luminescence decay for Bmpip₂PbBr₄ (two spectrally overlapping triplets, blue curve), Bmpip₂SnBr₄ (singlet and triplet, red curves) and Bmpip₂GeBr₄ (singlet and triplet, biexponential, orange curves). Singlet emission from Bmpip₂PbBr₄ is observed only with streak camera (see Figure S9) due to its fast decay (sub-50 ps). Black curves show exponential fit.

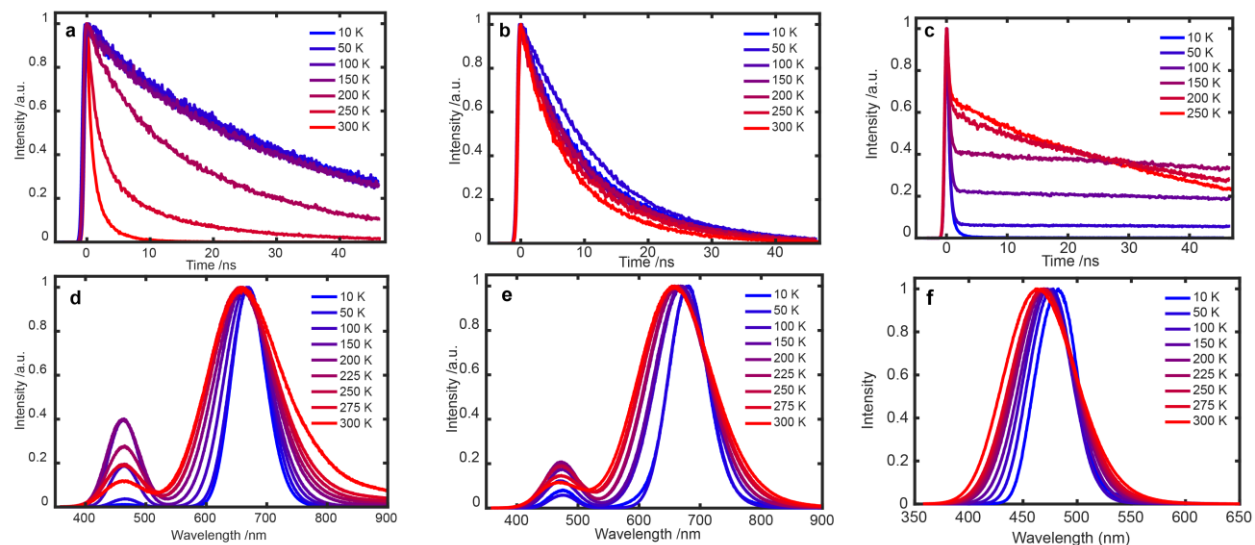


Figure S6. (a-b) Temperature-dependent emission decay curves for the singlet emission at 475 nm for Bmpip₂GeBr₄ and Bmpip₂SnBr₄. (c) Temperature-dependent emission decay curves for the emission peak at 470 nm for Bmpip₂PbBr₄. (d-f) Temperature-dependent normalized steady-state PL spectra under 310 nm laser excitation for Bmpip₂GeBr₄, Bmpip₂SnBr₄, Bmpip₂PbBr₄.

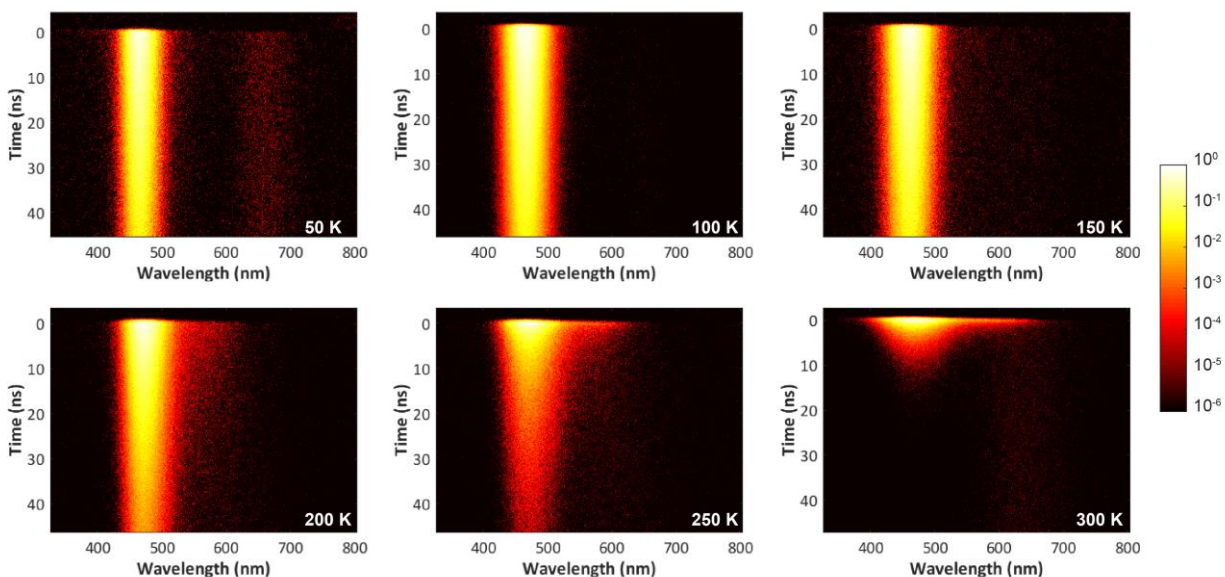


Figure S7. Time-resolved emission for Bmpip₂GeBr₄, collected with a streak camera at different temperatures.

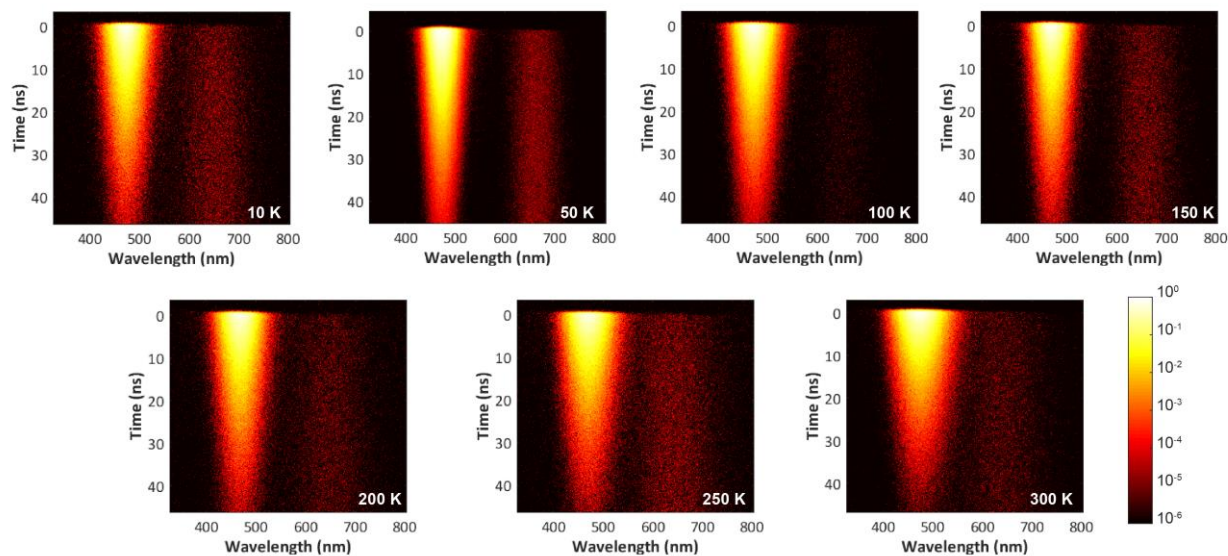


Figure S8. Time-resolved emission for Bmpip₂SnBr₄ collected with a streak camera at different temperatures.

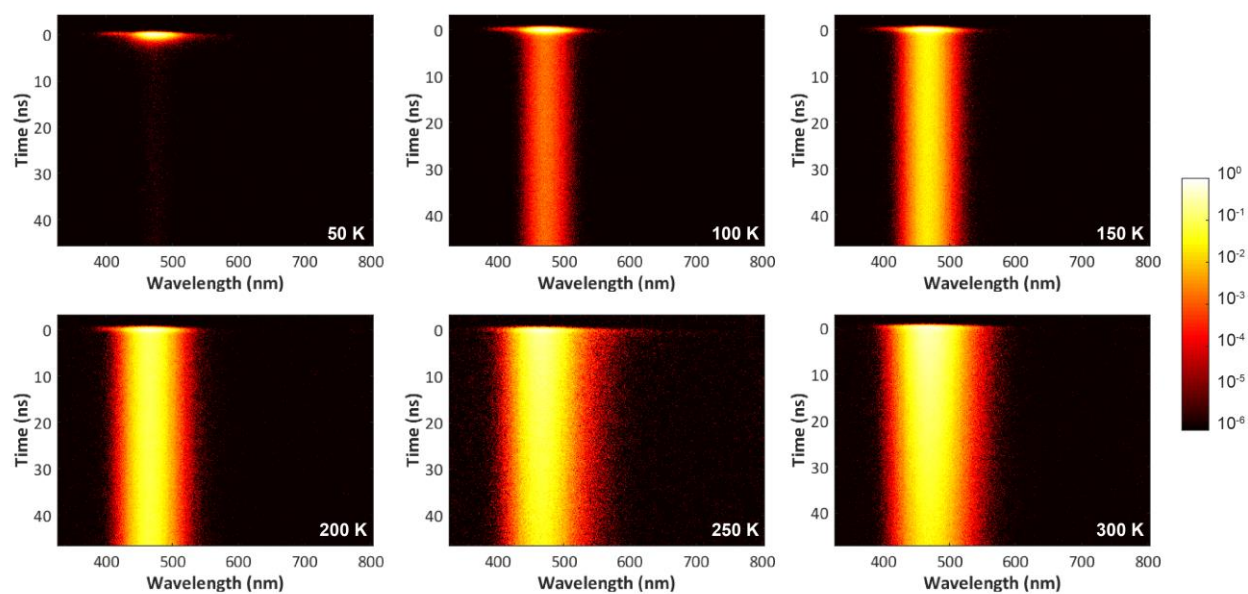


Figure S9. Time-resolved emission for Bmpip₂PbBr₄, collected with a streak camera at different temperatures in the 50 ns time window.

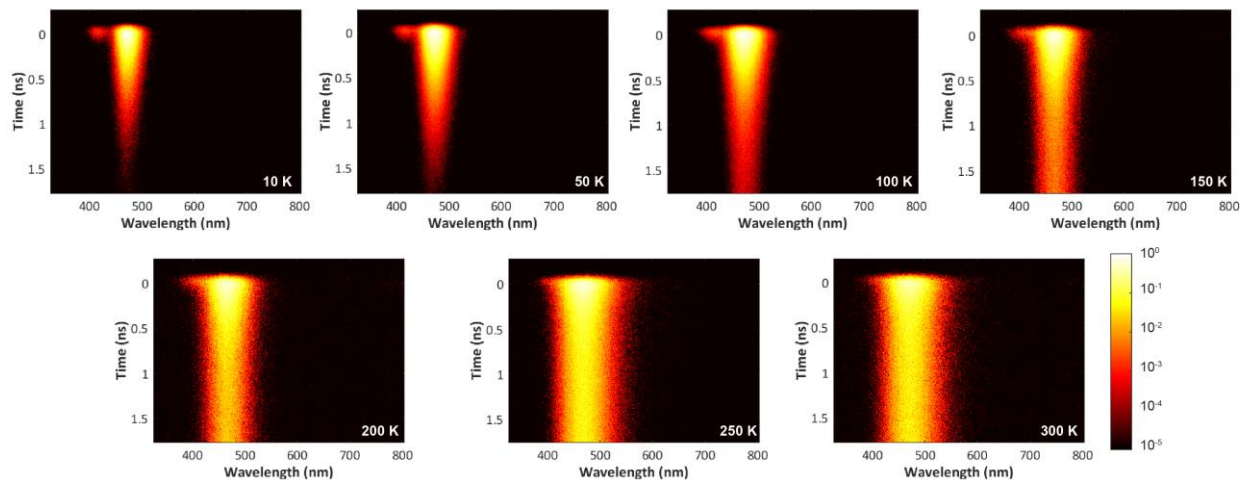
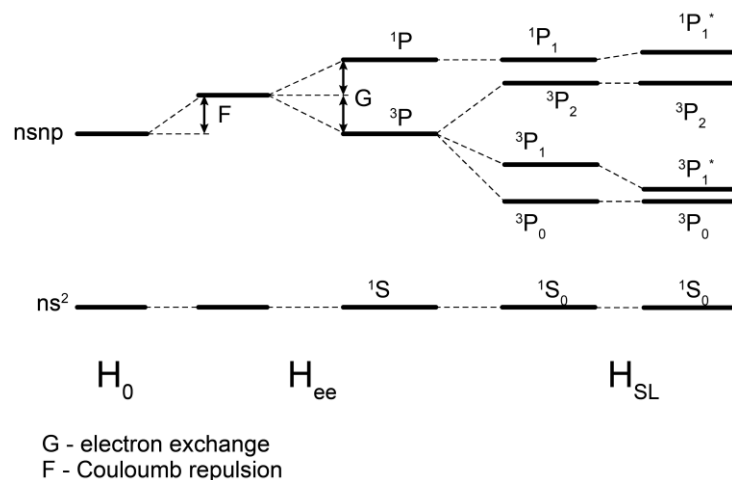


Figure S10. Time-resolved emission for Bmpip₂PbBr₄, collected with a streak camera at different temperatures in the 2 ns time window.



Scheme S1. Energy level diagram for an isolated ns^2 ion. Electron-electron interactions result in the Coulomb repulsion F and exchange interaction G . The diagonal terms in the spin-orbit coupling Hamiltonian H_{SL} (Russell-Saunders coupling) split the 3P term into its three components with $J=0,1,2$. The off-diagonal elements of H_{SL} mix 1P_1 and 3P_1 .⁸

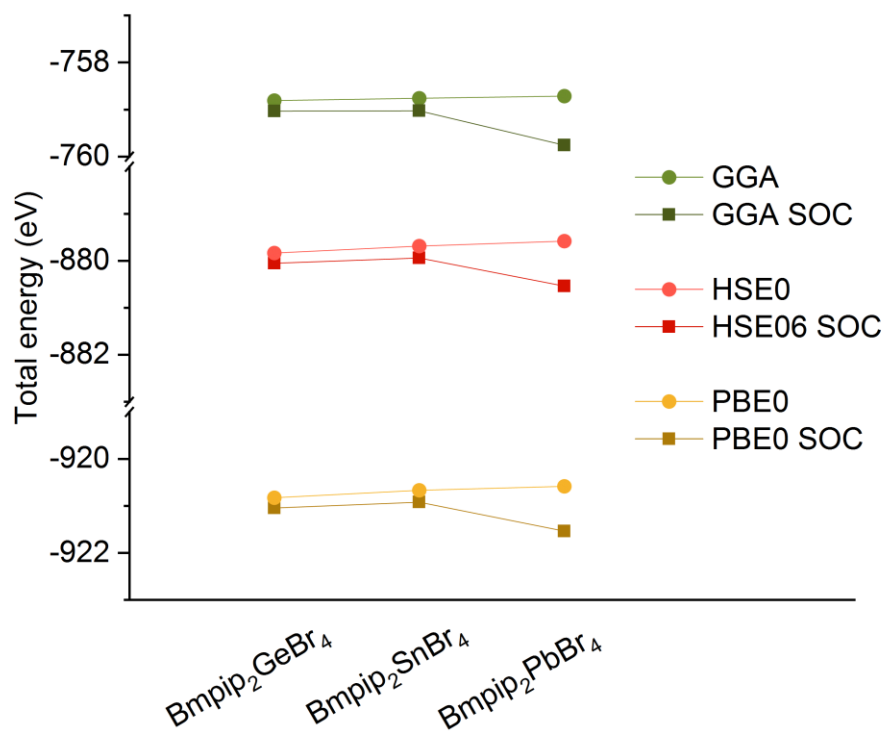


Figure S11. Comparison of total energy for Bmpip₂GeBr₄, Bmpip₂SnBr₄ and Bmpip₂PbBr₄ calculated with different functionals (GGA (PBE) or hybrid (PBE0 and HSE06)) without and with inclusion of SOC. The SOC inclusion in calculation only influences the total energy in case of Bmpip₂PbBr₄.

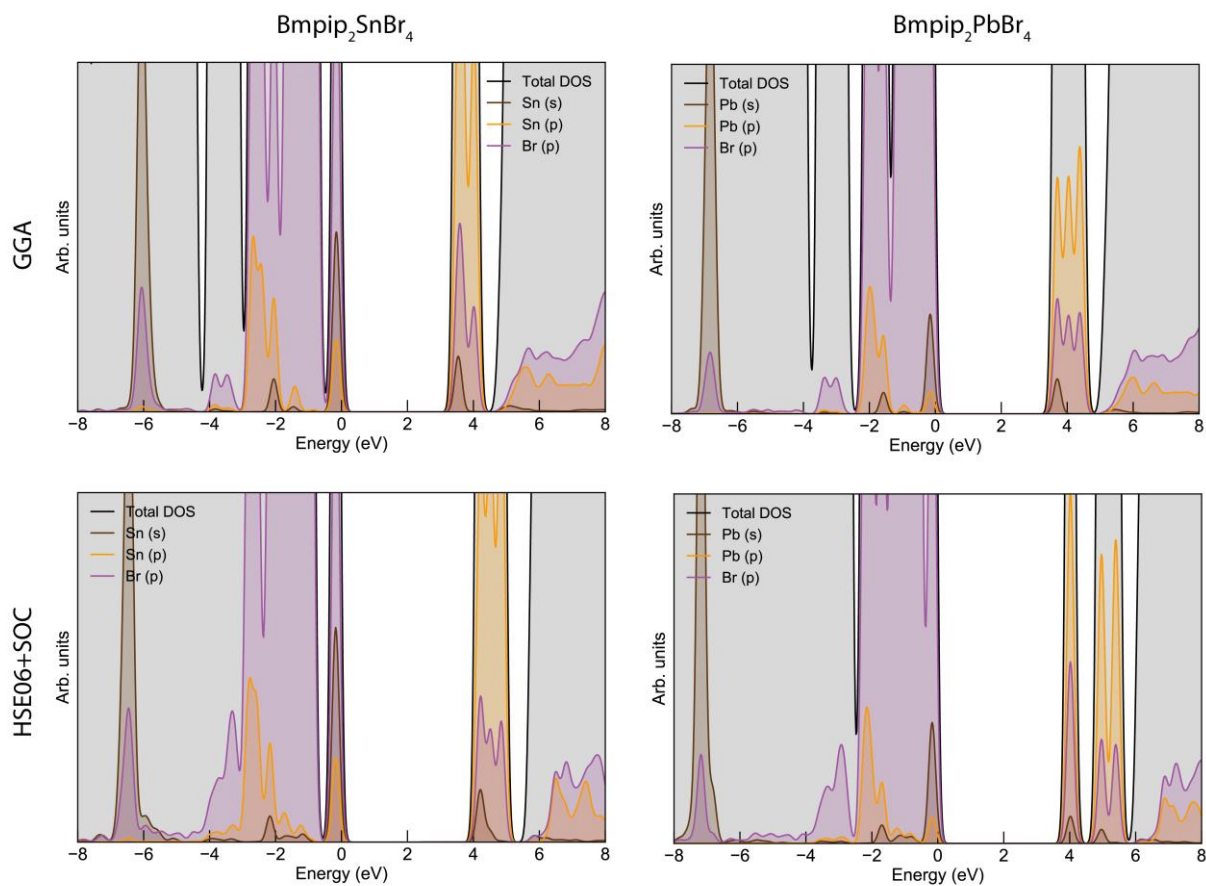


Figure S12. Comparison of DOS for Bmpip₂SnBr₄ and Bmpip₂PbBr₄ calculated with GGA and with HSE06+SOC. The contribution of metal *s*-orbitals to the top of the VB increases both for Sn and Pb.

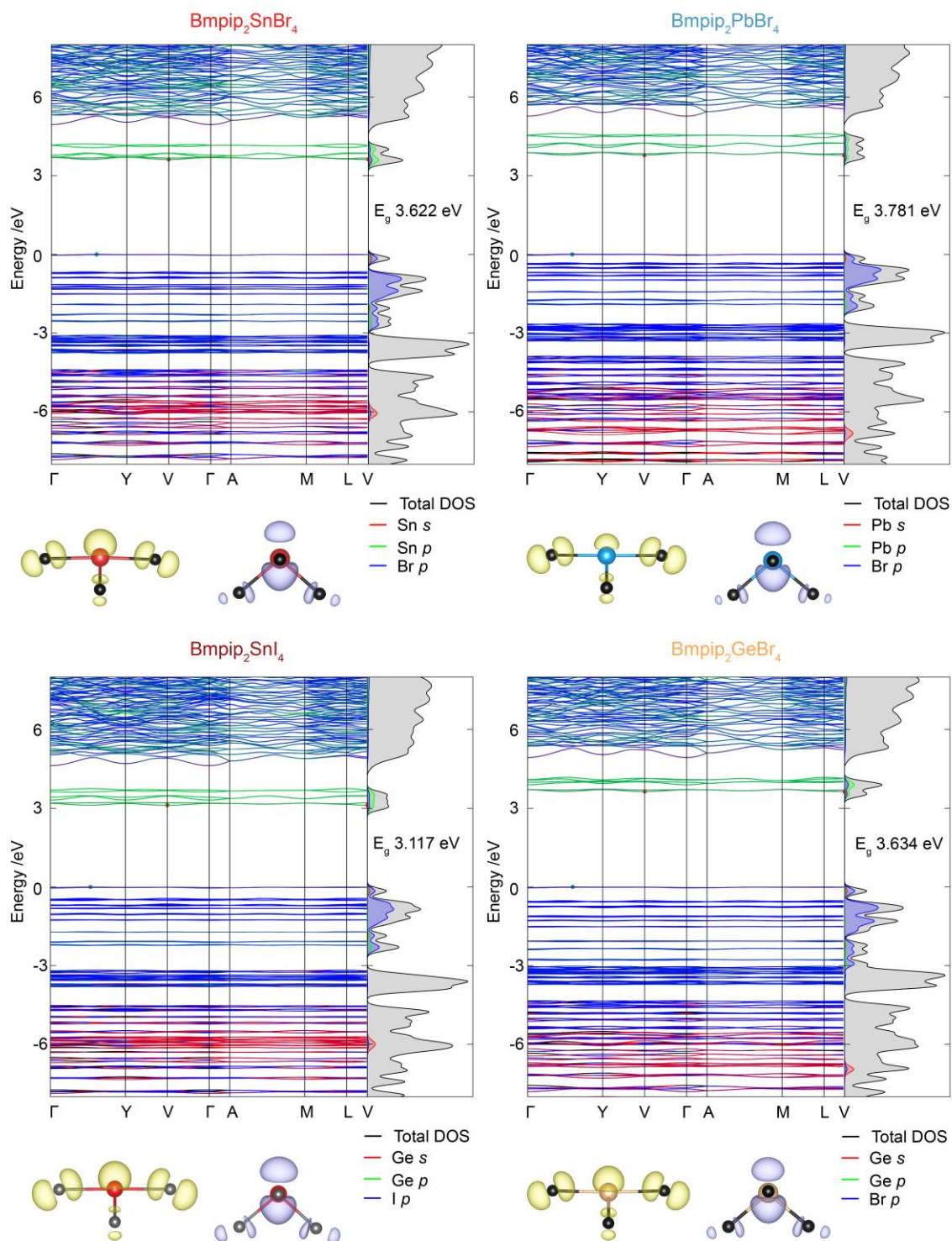


Figure S13. Orbital projected band structure and DOS of $\text{Bmpip}_2\text{SnBr}_4$, $\text{Bmpip}_2\text{PbBr}_4$, $\text{Bmpip}_2\text{SnI}_4$ and $\text{Bmpip}_2\text{GeBr}_4$. Yellow contour plot shows atom-projected hole wave-function localization at the top of the valence band between Γ and Y; purple contour plot shows electron wave-function localization at the bottom of the conduction band at point V.

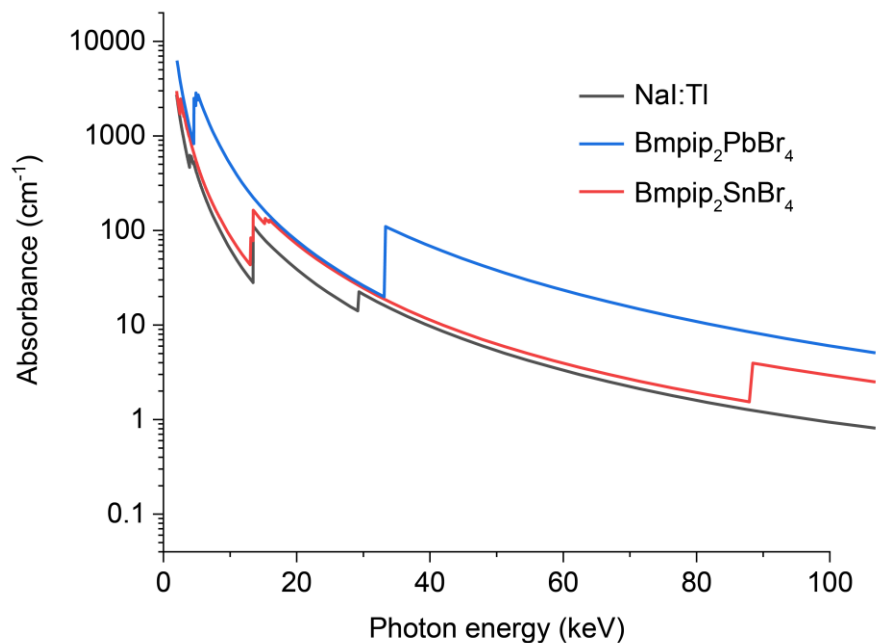


Figure S14. X-ray absorbance vs. photon energy for NaI, Bmpip₂PbBr₄, Bmpip₂SnBr₄. Calculated using NIST X-ray form factor, attenuation, and scattering tables.⁹

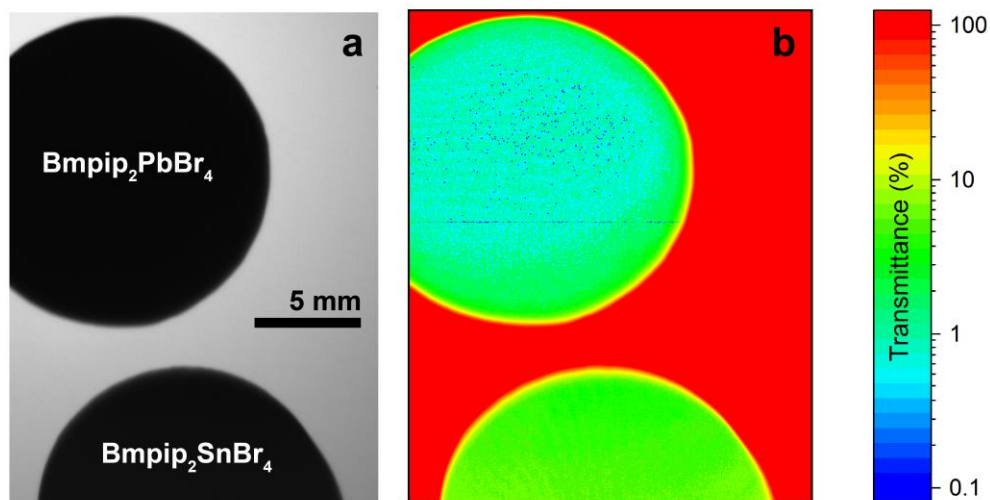


Figure S15. (a) Transmission image in X-rays of Bmpip₂PbBr₄ and Bmpip₂SnBr₄ obtained with RadEye HR sensor module. (b) Calculated transmittance, showing that pellets absorb more than 90% of the incident X-ray.

References

1. Sheldrick, G. M., Crystal Structure Refinement with SHELXL. *Acta Crystallogr. C* **2015**, *71*, 3-8.
2. Dolomanov, O. V.; Bourhis, L. J.; Gildea, R. J.; Howard, J. A. K.; Puschmann, H., OLEX2: a Complete Structure Solution, Refinement and Analysis Program. *J. Appl. Crystallogr.* **2009**, *42*, 339-341.
3. Blochl, P. E., Projector Augmented-Wave Method. *Phys. Rev. B* **1994**, *50* (24), 17953-17979.
4. Perdew, J. P.; Burke, K.; Ernzerhof, M., Generalized Gradient Approximation Made Simple. *Phys. Rev. Lett.* **1997**, *78* (7), 1396-1396.
5. Gunnarsson, O.; Lundqvist, B. I., Exchange and Correlation in Atoms, Molecules, and Solids by Spin-Density Functional Formalism. *Phys. Rev. B* **1976**, *13* (10), 4274-4298.
6. M Ganose, A.; Jackson, A.; Scanlon, D., sumo: Command-Line Tools for Plotting and Analysis of Periodic ab Initio Calculations. *The Journal of Open Source Software* **2018**, *3*, 717.
7. (a) Krukau, A. V.; Vydrov, O. A.; Izmaylov, A. F.; Scuseria, G. E., Influence of the Exchange Screening Parameter on the Performance of Screened Hybrid Functionals. *J. Chem. Phys.* **2006**, *125* (22); (b) Perdew, J. P.; Ernzerhof, M.; Burke, K., Rationale for mixing exact exchange with density functional approximations. *J. Chem. Phys.* **1996**, *105* (22), 9982-9985.
8. Jacobs, P. W. M., Alkali-Halide Crystals Containing Impurity Ions with the ns^2 Ground-State Electronic Configuration. *J. Phys. Chem. Solids* **1991**, *52* (1), 35-67.
9. Chantler, C. T., Detailed Tabulation of Atomic Form Factors, Photoelectric Absorption and Scattering Cross Section, and Mass Attenuation Coefficients in the Vicinity of Absorption Edges in the Soft X-ray ($Z=30-36$, $Z=60-89$, $E=0.1$ keV-10 keV), Addressing Convergence Issues of Earlier Work. *J. Synchrotron Radiat.* **2001**, *8*, 1124-1124.